

Higher-Order Implicit Large Eddy Simulations of a VFE-2 Delta Wing

Tarik Dzanic* and Luigi Martinelli†
Princeton University, Princeton, NJ 08540, USA

In this study, higher-order flux reconstruction methods are used to simulate the flow around a medium and large-radius VFE-2 delta wing using PyFR. The objective of the study was to validate the ability of higher-order methods to accurately predict blunt leading edge separation and adequately resolve vortex dynamics and to compare this approach to standard Reynolds-Averaged Navier-Stokes (RANS) approaches. Wall-resolved implicit large eddy simulations with fourth-order spatial and temporal accuracy were validated against experimental data for a medium-radius wing at a Reynolds number of $1 \cdot 10^6$ with very good agreement. Higher-order simulations of a large-radius wing at a Reynolds number of 40,000 were then compared to RANS simulations with two turbulence models. Noticeable differences in the computed flow structures and turbulence quantities were observed between the three methods along with minor differences in the predicted surface pressure distribution.

I. Nomenclature

α	= angle of attack
c	= root chord
C_P	= pressure coefficient
C_{PT}	= total pressure coefficient
η	= nondimensional semispan
M	= Mach number
Ω	= vorticity tensor
Q	= Q-criterion
Re_{mac}	= Reynolds number with respect to mean aerodynamic chord
ρ	= density
S	= rate-of-strain tensor
TKE	= turbulent kinetic energy
τ'	= Reynolds stress tensor
u	= streamwise velocity component
U_∞	= freestream velocity
v	= vertical velocity component
w	= spanwise velocity component
x	= streamwise direction
y	= vertical direction
z	= spanwise direction

II. Introduction

Due to the demand for highly-maneuverable and agile aircraft, slender delta wings have been the subject of many experimental and numerical studies owing to their desirable aerodynamic characteristics at high speeds and high angles of attack. The flow field over a slender delta wing is dominated by a pair of primary vortices above the upper surface of the wing caused by the separation of the flow near the leading edge. The entrainment and separation of the fluid by the primary vortices give rise to secondary vortices outboard of the primary vortices. Likewise, this effect can

*Undergraduate Student, Department of Mechanical and Aerospace Engineering, Princeton University, Princeton, NJ; Student Member, AIAA.
†Associate Professor, Department of Mechanical and Aerospace Engineering, Princeton University, Princeton, NJ; Associate Fellow, AIAA.

cause the generation of tertiary vortices as a result of the secondary vortices. As the angle of attack is increased, the strength of the vortices increases and the pressure at the upper surface of the wing decreases. When the angle of attack becomes sufficiently high, vortex breakdown occurs with the rapid deceleration of the tangential and axial components of the vortex flow and the expansion of the vortex core [1].

It is generally accepted that following the formation of the vortices at angles of attack prior to vortex breakdown, vortex dynamics can be adequately modeled with inviscid nonlinear models. Inviscid flow solvers or underresolved viscous flow solvers can be used to accurately compute the flow of the primary vortices for geometries for which the separation line is fixed by geometric discontinuities (e.g. sharp leading edge). However, practical considerations make the use of sharp leading edges in aircraft infeasible, and a rounded leading edge is required. Without geometric discontinuities, the primary vortices of rounded leading edge delta wings are instead formed as a result of the separation of the boundary layer near the leading edge, which leads to the roll-up of the shear layer and subsequent vortex formation. This process is controlled by momentum transport, which is extremely sensitive to the Reynolds number; failure to properly model this flow feature causes inaccurate predictions of the strength of the vortex system and the details of the flow field, which may even lead to inaccurate calculation of the aerodynamic forces.

In an attempt to gain insight on the more complex flow physics of rounded leading edge delta wings, the Second International Vortex Flow Experiment (VFE-2) was established consisting of a slender delta wing with 65° sweep and varying leading edge radii. Chu & Luckring defined the wing geometry and performed the initial experiments at the National Transonic Facility at NASA Langley [2]. Several groups have since then provided more comprehensive experimental data for the VFE-2 configuration at varying Reynolds numbers, Mach numbers, leading edge radii, and angles of attack [3–5]. These experiments serve to develop the understanding of vortex dominated flows and as a validation for numerical tools. As such, a significant number of numerical studies have been performed on the VFE-2 configuration [6–10].

Computational fluid dynamics (CFD) methods based on steady Reynolds-Averaged Navier-Stokes equations (RANS) are the prevailing model of choice in the industry. The system of RANS equations closed with well-calibrated turbulence models such as the Spalart-Allmaras and Menter SST turbulence models is usually discretized using second order numerical methods and integrated to a steady state [11, 12]. The use of lower-order methods introduces non-negligible amounts of numerical dissipation in the solution. As such, the computed vorticity field is artificially diffused, and the small-scale flow features such as secondary or tertiary vortices may not be adequately resolved. In addition, the turbulence models most commonly used for closure assume the velocity fluctuation correlations are isotropic, an assumption that is not justifiable for flows influenced by mean rotational effects as seen in the vortical structures over delta wings. To remedy some of these shortcomings, recent research has been directed toward the development of time resolved unsteady RANS (URANS) and Detached Eddy Simulation (DES) models [7, 9, 10]. But while URANS and DES models may be able to improve the resolution of the flow physics away from solid walls, they are unable to accurately predict the primary flow separation near rounded leading edges as shown by both Crippa & Rizzi and Schiavetta, Badcock, & Cummings [9, 10].

Today's availability of massively-parallel GPU computing and its consequent significant increase in computational power allows for more accurate approaches to complex flow problems. Higher-order methods - defined as having an order of accuracy of 3 or higher - have shown promise as a numerical tool for high-fidelity simulations since they are less susceptible to the detrimental effects of excessive numerical dissipation on simulating fundamentally unsteady vortex dominated flows. In addition, higher-order methods offer increased accuracy for the same degrees of freedom (i.e. memory), an important feature in the limit of memory bandwidth constraints of GPU computing. A common approach to higher-order methods in CFD has been with discontinuous finite element methods such as the discontinuous Galerkin (DG) and flux reconstruction (FR) methods [13, 14]. These methods allow for an arbitrarily high order of accuracy that can be efficiently implemented on the current generation of hierarchical memory high performance computing (HPC) architectures.

In this work, higher-order methods based on flux reconstruction are used to simulate the flow around a medium-radius and large-radius leading edge VFE-2 delta wing. The approach used is commonly known as implicit Large Eddy Simulation (ILES) in which no subgrid-scale (SGS) model is explicitly added to the discretized Navier-Stokes equations while subgrid modeling is accomplished by the numerical truncation error [15]. The approach is validated with wall-resolved ILES results against experimental VFE-2 data obtained by the Institute of Aerodynamics (AER) of the Technische Universität München (TUM) for the medium-radius leading edge at a Reynolds number of $1 \cdot 10^6$ based on the mean aerodynamic chord [3]. Furthermore, wall-resolved ILES results are presented for the more complex flow physics of the large-radius leading edge at a Reynolds number of 40,000 and the computed time-averaged flow structure is compared with the results of RANS simulations.

III. Computational Approach

A. Geometry and Flow Conditions

The geometry consisted of a VFE-2 delta wing with a leading edge radius to mean aerodynamic chord ratio of 0.15% and 0.30% corresponding to the medium-radius and large-radius set, respectively, of the initial experimental data by Chu & Luckring. The sting and fairing from the experimental model were not included. For the medium-radius, a Reynolds number of $1 \cdot 10^6$ based on the mean aerodynamic chord and freestream viscosity was chosen with an angle of attack of 18° corresponding to the TUM-AER experimental data for “fully-developed leading-edge vortices”. However, the simulated Mach number ($M = 0.2$) was higher than the experimental Mach number ($M = 0.07$) to allow for efficient use of the compressible solver.

For the large-radius, a Reynolds number of 40,000 based on the mean aerodynamic chord and freestream viscosity was chosen as fully-resolved simulations at the experimental Reynolds number of $6 \cdot 10^6$ by Chu & Luckring were not feasible. The flow conditions corresponding to the data set at a Mach number of 0.4 and an angle of attack of 12.3° were applied. These conditions allowed for well-developed vortices while maintaining subsonic flow to avoid the detrimental effects of shocks on solver stability and accuracy.

B. Solver

The compressible Navier-Stokes equations were solved using the flux reconstruction method in PyFR v1.7.5 with fourth-order spatial and temporal accuracy using the Roe-FDS and LDG schemes [16–18]. The simulations were impulsively started and run until a nondimensional time of 2.5, corresponding to two and a half flows over root chord. The solution was approximated with $P3$ polynomials along Gauss-Legendre points for hexahedral elements and quadrilateral faces and Williams-Shunn points for prismatic elements and triangular faces. Viscosity correction was applied using Sutherland’s law. A wall-resolved ILES approach was used with no turbulence modeling, and an explicit four-stage Runge-Kutta method was used for time stepping with nondimensional time steps of $1 \cdot 10^{-7}$ and $8 \cdot 10^{-7}$ for the medium-radius and large-radius, respectively. Anti-aliasing by means of the L^2 projection of the divergence flux with a quadrature degree of 9 was used for stabilizing. A half delta wing was simulated with an inviscid wall symmetry plane. Characteristic Riemann invariant boundary conditions were applied to the farfield, and the wing surface was assigned an adiabatic no-slip wall boundary condition.

Solving was performed on the Tiger2 GPU cluster at the TIGRESS High Performance Computing Center at Princeton University across 32 nVidia P100 GPUs with an estimated computing power of 150 double precision TFLOPs. The solving time to complete two and a half flows over root chord was approximately 90 hours for the large-radius and 15 days for the medium-radius.

The results of the ILES solver for the large-radius were compared to the results of the steady-state compressible RANS solutions given by ANSYS Fluent and STAR-CCM+. A second-order upwinding approach was used for both the flow and turbulence variables, and Sutherland’s law was used for viscosity correction. The Menter SST turbulence model was used with ANSYS Fluent as it behaves well within regions of separated flow and allows for direct comparison of modeled turbulent kinetic energy to ILES resolved turbulent kinetic energy. The Elliptic Blending Reynolds Stress Model (EBRSM) was used with STAR-CCM+ for comparison of the modeled and ILES resolved Reynolds stress components [19].

Geometry	Computational Method	Re_{mac}	M	α
Medium-radius	ILES (4th order)	$1 \cdot 10^6$	0.2	18°
Large-radius	ILES (4th order)	40,000	0.4	12.3°
Large-radius	RANS-SST (2nd order)	40,000	0.4	12.3°
Large-radius	RANS-EBRSM (2nd order)	40,000	0.4	12.3°

Table 1 Simulation test matrix

C. Mesh

1. Higher-Order Mesh Elements

As higher-order finite element methods rely on increasing the order of the solution approximation within the element, the mesh is significantly coarser than finite volume meshes of comparable accuracy. This coarsened mesh must still accurately represent the geometry, or the benefits of higher-order methods are forfeited. Linear meshes, which represent the geometry as first order C_0 continuous curves, are adequate for finite volume methods as the second-order error introduced by the linear representation of the geometry is of the same magnitude or lower as the solution error. For higher-order methods with geometries where curvature plays a significant role on the flow field, higher-order mesh elements must be used. These mesh elements are represented by polynomials of degree 2 or higher. Solution points are then added along the higher-order polynomial curve, and the boundary conditions are enforced with respect to the higher-order representation of the geometry, taking into account for the effects of curvature.

2. Mesh Generation

Three meshes were generated, two for the ILES solver (medium-radius and large-radius) and one for the RANS solvers (large-radius). The wing surface mesh consisted of an unstructured flat-plate region and a structured leading/trailing edge region. Edge biasing was performed towards the leading and trailing edges. The surface mesh was extruded normal to the surface for the blunt wing up to 10% of the root chord to obtain a high-orthogonality prismatic/hexahedral region near the wall. Subsequently, the mesh was extruded until the farfield along the coordinate axes. The farfield is defined as $x = [-10, 15]$, $y = [-15, 15]$, $z = [0, 15]$ for a streamwise x direction and spanwise z direction.

For the ILES meshes, the wall-normal resolution was dictated by the size of the viscous sublayer: the first mesh cell lies within $y^+ < 5$ at all points along the wing surface based on the flat-plate boundary layer at the respective Reynolds numbers with the first Gauss-Legendre solution point at $y^+ \approx 1.5$. As such, the ILES meshes were fully wall-resolved. The y^+ estimate was confirmed a posteriori with direct calculations of the wall shear stress. The wall-tangent mesh sizing was dictated by the stability requirements of the ILES solver. Aspect ratios greater than approximately 10 in areas of large gradients caused uncontrollable instabilities. With the $P3$ solution, the number of degrees of freedom of the ILES meshes was approximately 16 million for the medium-radius and 25 million for the large-radius.

For the large-radius RANS mesh, due to the reduced computational resource requirements and number of solution points, a significantly finer mesh was generated. The nodes of the RANS mesh were approximately equally spaced as the solution points of the ILES mesh in the wall-tangential directions, but the wall-normal direction was significantly more resolved with $y^+ < 1$ based on a flat-plate boundary layer at $Re = 40,000$. However, even with the increased wall resolution, the number of solution points, 12 million, was less than the ILES mesh as the RANS solvers were less susceptible to cell growth rate driven instabilities.

For the ILES meshes, linear mesh elements were originally generated in Pointwise, and then the elements were converted into second order elements with C_1 continuity using meshCurve by a fourth-order interpolation of the surrounding surface nodes [20]. Feature curves, acting as barriers to the interpolation stencil, were marked for the trailing edges and the interface between the flat plate and leading/trailing edge region. For the RANS mesh, linear elements were sufficient for the lower-order solvers.

D. Post-Processing and Data Analysis

Post-processing was performed in Paraview for field and cross-section data. After two nondimensional time units, the flow was assumed to be fully developed. Statistical quantities were acquired and analyzed from 2 to 2.5 time units. Pressure coefficient plots were obtained by interpolating the nearest solution points. Statistics on the turbulent behavior of the flow were also gathered, particularly the six independent quantities of the Reynolds stress tensor

$$\tau' = \bar{\rho} \begin{bmatrix} \overline{u'u'} & \overline{u'v'} & \overline{u'w'} \\ \overline{v'u'} & \overline{v'v'} & \overline{v'w'} \\ \overline{w'u'} & \overline{w'v'} & \overline{w'w'} \end{bmatrix}, \quad (1)$$

the turbulent kinetic energy (TKE)

$$TKE = \frac{1}{2}(\overline{u'}^2 + \overline{v'}^2 + \overline{w'}^2), \quad (2)$$

and the averaged root mean square (RMS) values of the velocity fluctuations

$$\overline{u}'_{i,RMS} = \sqrt{\overline{u'^2_i}} \quad (3)$$

where the subscript i denotes the component of the velocity vector. The turbulence statistics are plotted nondimensionalized by the freestream velocity and density. 1000 data samples were taken in the time range, which resulted in means of the fluctuations that were strictly less than 1% of the maximum fluctuation for all sampled points. To visualize the vortical flows, isovolumes of the Q-criterion were generated. The Q-criterion was calculated as

$$Q = \frac{1}{2}(|\boldsymbol{\Omega}|^2 - |\mathbf{S}|^2) \quad (4)$$

where $\boldsymbol{\Omega}$ is the vorticity tensor and \mathbf{S} is the rate-of-strain tensor.

For comparison of the simulation results and experimental data, the simulation results were transformed into the coordinate system of the experimental data. For the velocity field visualization given by stereo particle image velocimetry, the vertical velocity component is taken with respect to the wing surface normal, but for the turbulent flow quantities given by hot-wire anemometry, the vertical velocity component is taken with respect to the freestream flow. In this work, the vertical velocity component is denoted as v , whereas in the experiment it is denoted as w .

IV. Results

A. Medium-radius

1. Velocity Field

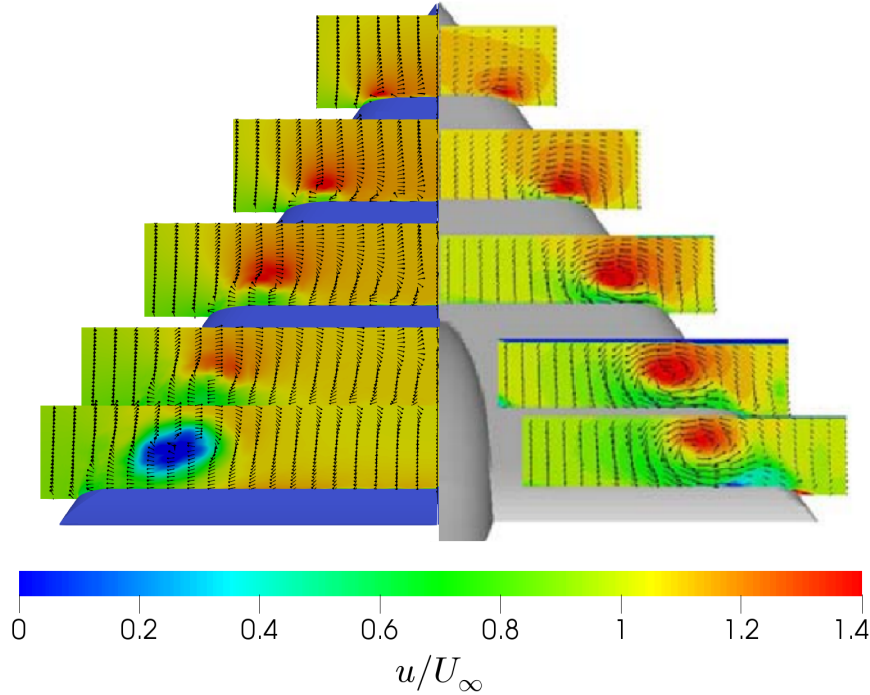


Fig. 1 Average streamwise velocity distribution with crossflow vectors for ILES (left) and experiment (right)

The time-averaged flow field obtained with ILES at cross-sections $x/c = 0.2, 0.4, 0.6, 0.8$, and 0.95 is shown in Fig. 1 in comparison to the time-average experimental flow field with the contours of streamwise velocity and vector plots of the spanwise and vertical velocity. For cross-sections $x/c = 0.2, 0.4$, and 0.6 , the ILES results and experimental data show great agreement in both the magnitude and lateral and vertical positioning of the region of increased streamwise velocity corresponding to the primary vortex core. However, at cross sections $x/c = 0.8$ and 0.95 , the ILES results show a significant deceleration in the streamwise velocity in the vortex core and the elliptic deformation of the vortex core which is characteristic of the onset of vortex breakdown, whereas in the experimental results, no such deceleration is noticed. This is particularly evident at $x/c = 0.95$ where the axial velocity of the vortex core in ILES is underpredicted by over a factor of 3 in comparison to the experimental results.

Although it initially appears as though the flow physics predicted by the ILES method significantly deviate from the experiment near the trailing edge, it must be noted that in the experiment, the flow field at $\alpha = 18^\circ$ was particularly sensitive: the placement of a miniature hot-wire probe near the trailing edge could promote premature vortex breakdown. It is feasible to assume that the sensitive nature of the flow conditions paired with the modified geometry in the trailing edge region is the cause of the premature prediction of vortex breakdown.

2. Surface Streamlines and Pressure Coefficient Plots

The surface streamlines of the time-averaged ILES flow with contours of pressure coefficient is shown in Fig. 2 in comparison to the experimental oil flow visualization. The ILES results and experimental data show notable similarities in the rollup and positioning of the primary vortex and the separation line of the secondary vortex, as well as the width of the primary vortex. In addition, the trailing edge separation is predicted in the same location with ILES as the experiment. The ILES prediction of the primary vortex position shows good agreement with the experiment even in the trailing edge region, indicating that the removal of the sting has minimal effect on the primary vortex position.

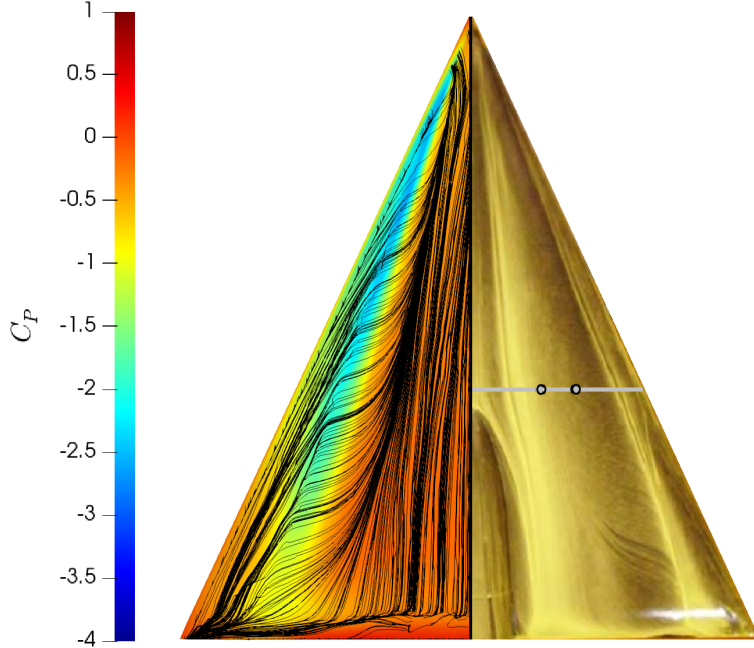


Fig. 2 Surface oil flow topology for ILES (left) and experiment (right)

A comparison of the pressure coefficient distribution at cross-sections $x/c = 0.2, 0.4, 0.6$, and 0.8 between the time-averaged ILES results and the experiment is shown in Fig. 3. Most notably, the ILES method accurately predicted the formation of the primary vortex and the lateral position of the vortex core at each streamwise station. The advantages of the wall-resolved higher-order methods used in this work over conventional wall-modeled LES is particularly evident with the accurate prediction of the formation of the primary vortex. At $x/c = 0.2$, the ILES results show very good agreement with the experiment for the position of the primary vortex, whereas the vortex position in the wall-modeled

LES approach in [21] deviated inboard of the experimental data by 20-50% of the local semispan.

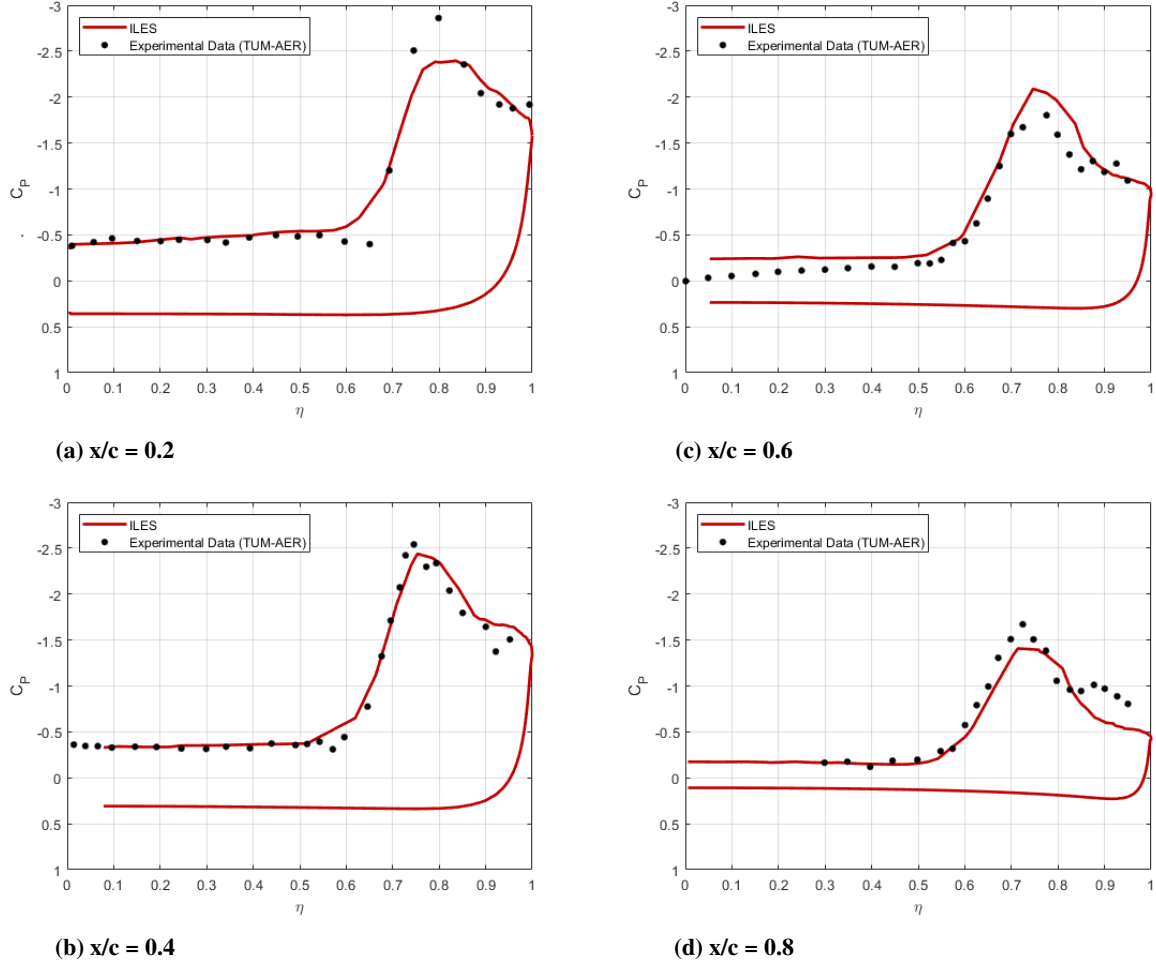


Fig. 3 Time-averaged surface pressure coefficient distribution for ILES and experiment

However, although the predicted positioning of the vortex core is in very good agreement with the experiment, some minor deviations in the predicted vortex strength are seen. At $x/c = 0.2$, the suction peak is underpredicted by roughly a factor of 15%, whereas at $x/c = 0.6$, the suction peak is overpredicted by roughly a factor of 10%. These effects can be attributed to the difference in Mach number between the simulation and the experiment. In [22], it was observed that at a constant Reynolds number and angle of attack, an increase in Mach number delayed blunt leading-edge separation. The difference in suction peak values at $x/c = 0.2$ can be attributed to a more developed primary vortex in the experiment as a result of the lower Mach number. At $x/c = 0.6$, the deviation in suction peak values matched the trend observed in [3] from comparison of experimental data at $M = 0.14$ and $M = 0.2$ at the same streamwise location. The increase in Mach number caused a stronger suction peak and pushed the vortex core slightly outboard, similar to Fig. 3 (c).

3. Turbulent Flow Quantities

The time-averaged root mean square values of the three components of the velocity fluctuations at cross-section $x/c = 0.6$ are shown in Fig. 4 for the ILES results and the experimental data. The predictions given by ILES were in overall good agreement with the experiment in terms of magnitude and distribution, although some deviation was seen with the spanwise velocity fluctuations. For the streamwise component, the experiment and the ILES results both showed a region of high fluctuation intensity at the vortex core and a smaller region of high fluctuation intensity near the leading edge. The high streamwise fluctuation intensity vortex core region was elliptically stretched with ILES in comparison to the circular region seen in the experiment. For the vertical component, the results given by ILES

were nearly identical to the experiment with a small region of high fluctuation intensity at the vortex core, but the ILES results contained another region of high vertical fluctuation intensity near the leading edge which was not observed in the experimental data. For the spanwise component, the region of high fluctuation intensity given by ILES was larger than the experiment, and the structure of the high fluctuation intensity region seen in the experiment akin to the rollup of the primary vortex could not be distinguished.

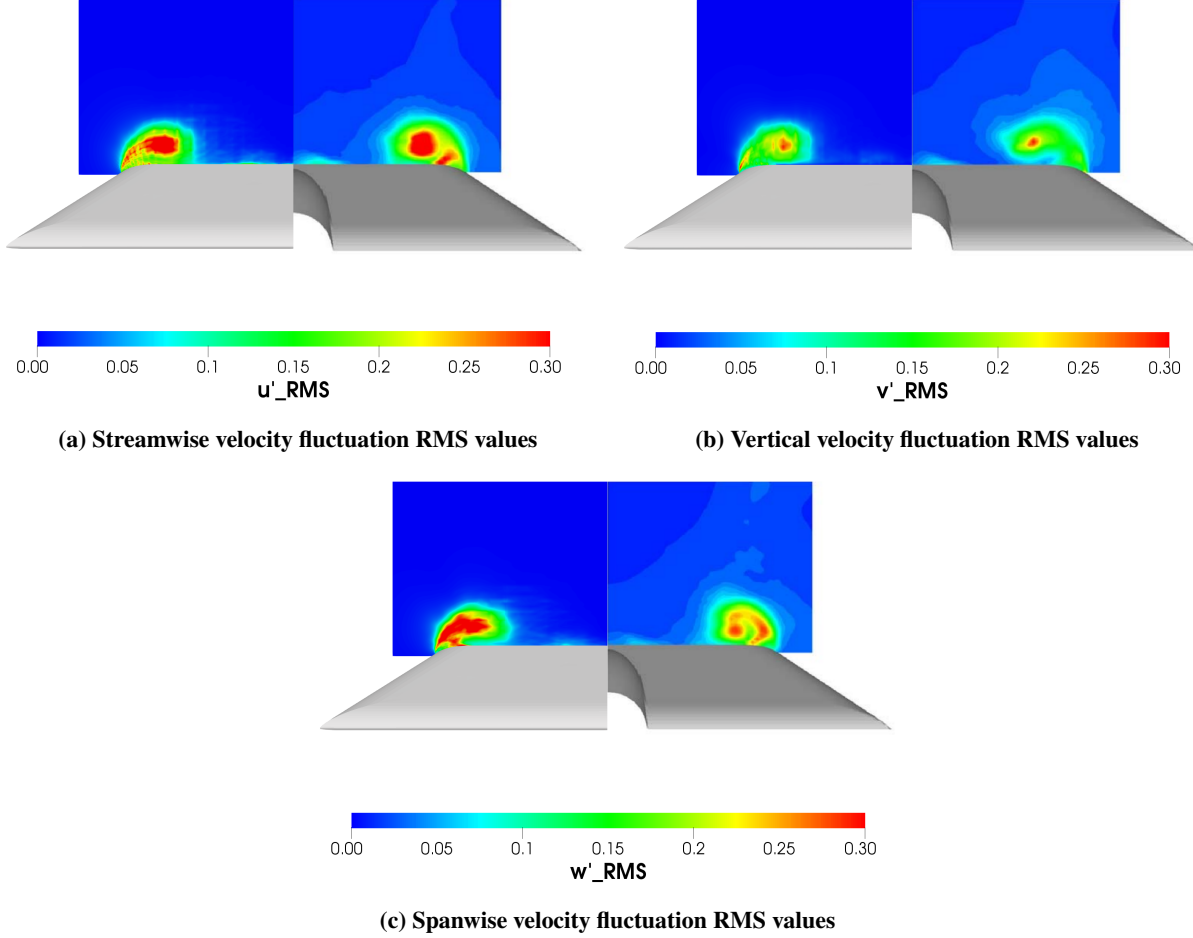


Fig. 4 Time-averaged turbulent fluctuation intensities for ILES (left) and experiment (right)

B. Large-radius

1. *Q*-criterion and Oil Flow

The computed average flow characteristics are shown with *Q*-criterion isovolumes and surface oil flow paths in Fig. 5 for the time-averaged ILES, RANS-SST, and RANS-EBRSM results. All three methods showed evident primary and secondary vortex separation and reattachment lines as well as trailing edge separation in the oil flow paths. The ILES oil flow showed tertiary vortex separation and reattachment lines whereas both RANS methods did not. The separation line for the primary and secondary vortices was predicted in similar locations with ILES and RANS-EBRSM, but was noticeably delayed with RANS-SST. The size of the primary vortex (visualized by the distance between the primary vortex reattachment line and the secondary vortex separation line) predicted by ILES was more compact than RANS-SST and of similar size to RANS-EBRSM. Conversely, the size of the secondary vortex predicted by ILES was similar to RANS-SST and more compact than RANS-EBRSM. Trailing edge separation was predicted prematurely with RANS-EBRSM and delayed with RANS-SST in comparison to ILES. Coherent primary and secondary vortices were seen in the *Q*-criterion isovolumes for all three methods, but the primary vortex structure was more compact with ILES.



Fig. 5 Q-criterion isovolumes colored by C_{PT} (left) and surface oil flow topology colored by C_P (right)

Overall, better agreement was observed between ILES and RANS-EBRSM than with ILES and RANS-SST in terms of flow structure and topology.

2. Total Pressure Cross-Sections

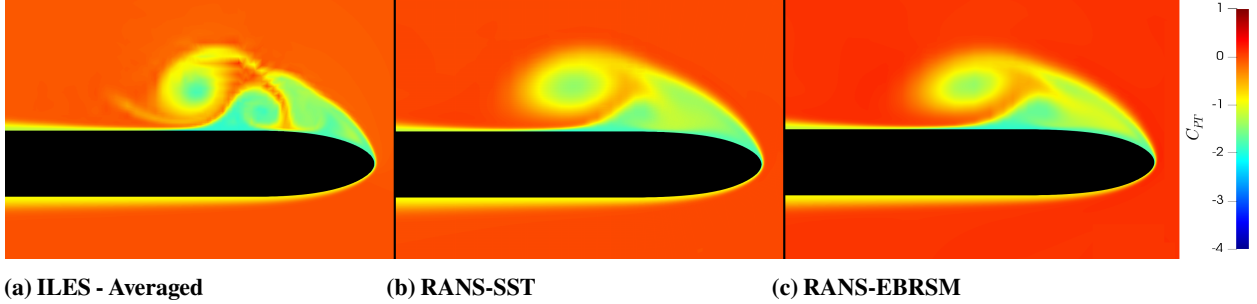


Fig. 6 Contours of total pressure coefficient at cross-section $x/c = 0.6$

The total pressure coefficient at cross-section $x/c = 0.6$ is shown in Fig. 6 for the time-averaged ILES, RANS-SST, and RANS-EBRSM methods. The flow fields computed by RANS-SST and RANS-EBRSM were nearly identical at this streamwise position and significantly differed from the ILES flow field. The positioning of the primary vortex core was similar between the three methods, although the flow fields computed by the RANS methods were more diffused than the ILES flow field and appeared to laterally stretch the primary vortex. The secondary vortex was not distinct and the tertiary vortex was not resolved in the RANS flow fields, whereas the ILES flow field distinctly resolved the secondary vortex and showed signs of the formation of the tertiary vortex. The curvature of the shear layer rollup of the secondary vortex was higher in the ILES flow field as a result of the lower pressures of the primary vortex core which resulted in a difference in positioning of the secondary vortex.

3. Surface Pressure Coefficient Plots

A comparison of the surface pressure coefficient with respect to the local semispan η at cross-sections $x/c = 0.2, 0.4, 0.6$, and 0.8 is shown in Fig. 7 for the time-averaged ILES, RANS-SST, and RANS-EBRSM methods. At all streamwise positions, the structure of the pressure coefficient distribution obtained by both RANS methods was similar,

but the RANS-EBRSM method consistently predicted the pressure coefficient to be more negative than RANS-SST on the suction side outboard of the primary vortex. At $x/c = 0.2$, the ILES and RANS-SST results were in very good agreement, but the RANS-EBRSM results were offset by roughly a factor of 10% across the entire span on the suction side. At the remaining streamwise positions, the primary vortex position was predicted at the same location by the three methods. However, better agreement was seen in the primary vortex suction peak magnitude between ILES and RANS-EBRSM at $x/c = 0.4$ and 0.6. At $x/c = 0.8$, the suction peak predicted by RANS-SST was closer to the ILES results than RANS-EBRSM. Additionally, the presence of a secondary vortex is visible in the ILES pressure coefficient distribution at $x/c = 0.4$, whereas it is not in the pressure coefficient distributions obtained by RANS-SST and RANS-EBRSM.

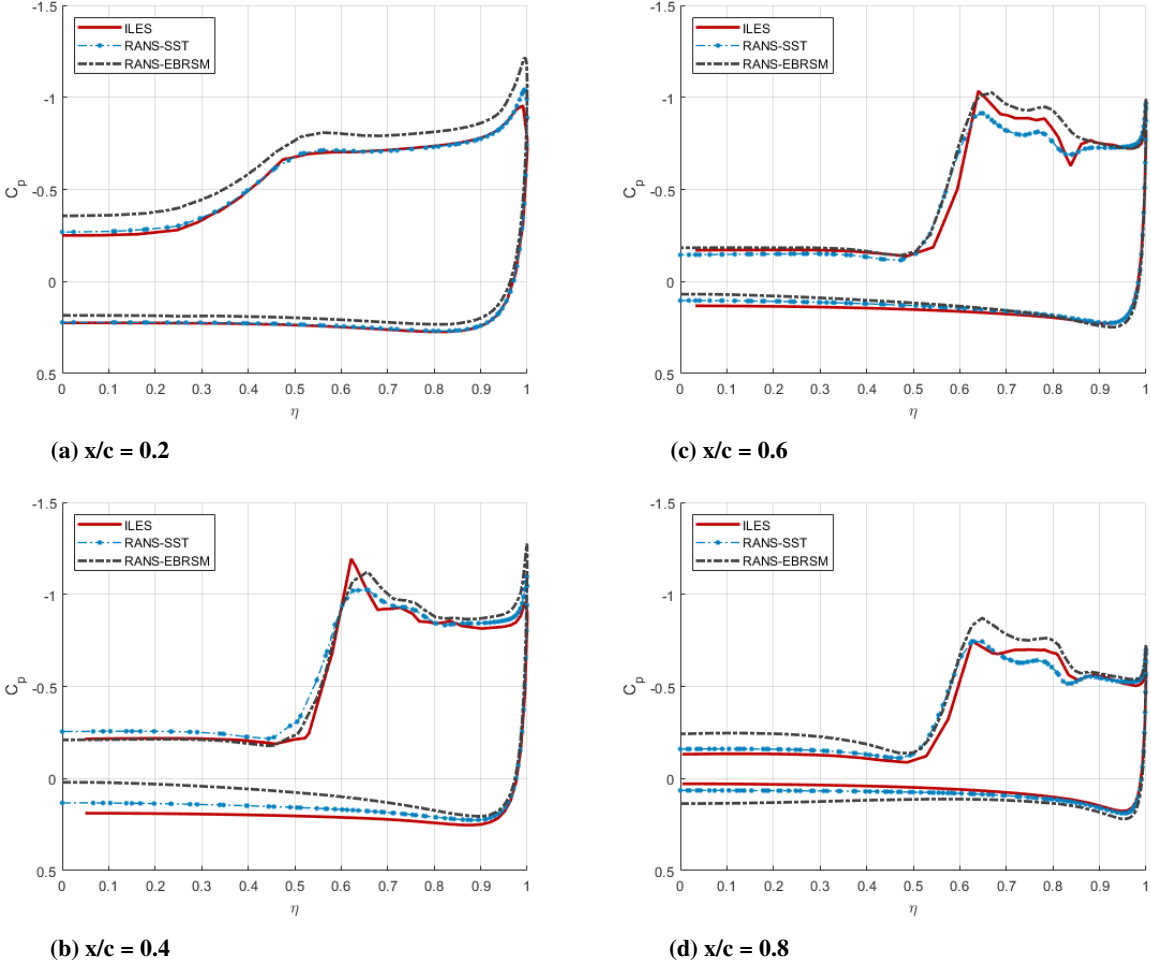


Fig. 7 Surface pressure coefficient distribution for time-averaged ILES, RANS-SST, and RANS-EBRSM

4. Turbulent Kinetic Energy Cross-Sections

A comparison of the turbulent kinetic energy at cross-sections $x/c = 0.8$ and 0.95 is shown in Fig. 8 for the time-averaged ILES, RANS-SST, and RANS-EBRSM methods. A significant difference in the TKE magnitude and distribution was seen between the RANS and ILES results. With the RANS methods, the magnitude of TKE was underestimated by a factor of two or more in comparison to ILES, with the most notable location being the primary vortex core. At $x/c = 0.8$, the structure of the TKE field was similar between the methods, although the field was significantly more diffused with RANS-SST than with ILES, and even more so with RANS-EBRSM. At $x/c = 0.95$, a region of high TKE was located at the primary vortex core in the ILES cross-section which was not evident in the cross-section from either RANS method, and the magnitude of TKE above the secondary vortex was severely

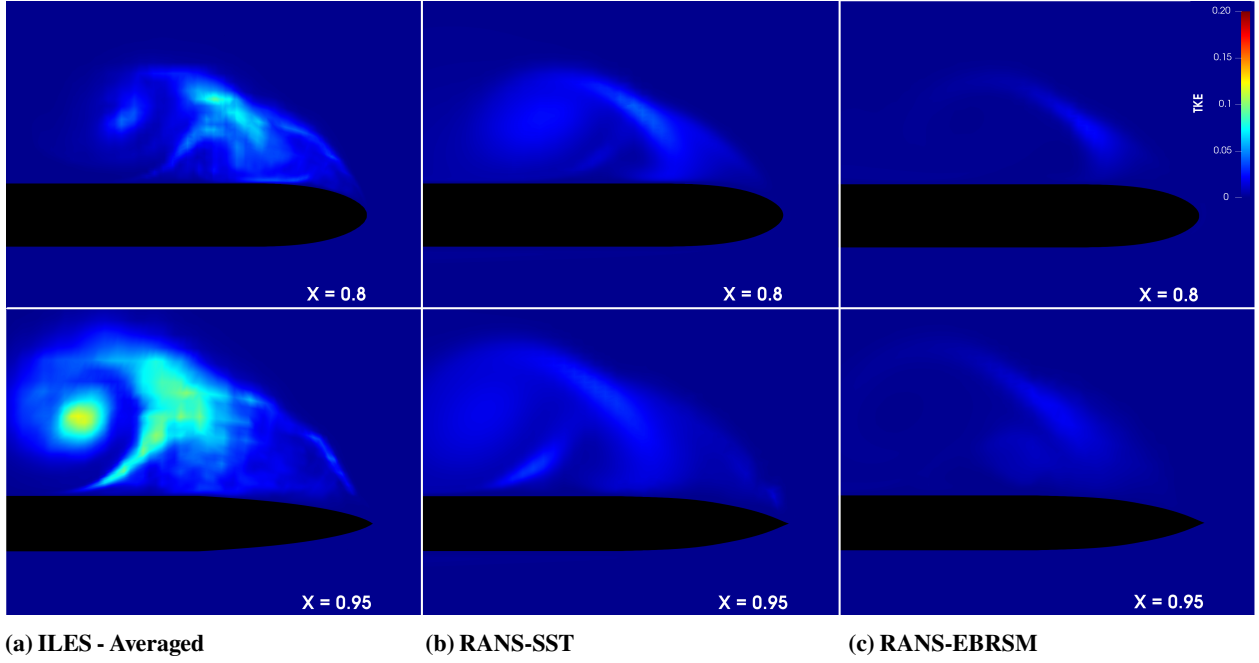


Fig. 8 Contours of turbulent kinetic energy at cross-sections $x/c = 0.8$ and 0.95

underpredicted by the RANS methods in comparison to ILES.

5. Reynolds Stress Cross-Sections

A comparison of the streamwise-spanwise ($\rho u' w'$) Reynolds stress at cross-section $x/c = 0.8$ is shown in Fig. 9 for the time-averaged ILES and RANS-EBRSM methods. The legend scale for the RANS-EBRSM contours is amplified by a factor of 5 with respect to the ILES contours as the RANS-EBRSM Reynolds stress was underpredicted by over an order of magnitude in comparison to ILES. A region of high positive Reynolds stress was seen in the ILES results above the secondary vortex and in the boundary layer below the tertiary vortex, and a negative Reynolds stress region was seen in the rollup of the primary vortex. The RANS-EBRSM results showed slight indication of the positive and negative Reynolds stress regions of the secondary and primary vortices, respectively, but the magnitude was severely underpredicted and the overall agreement was very poor.

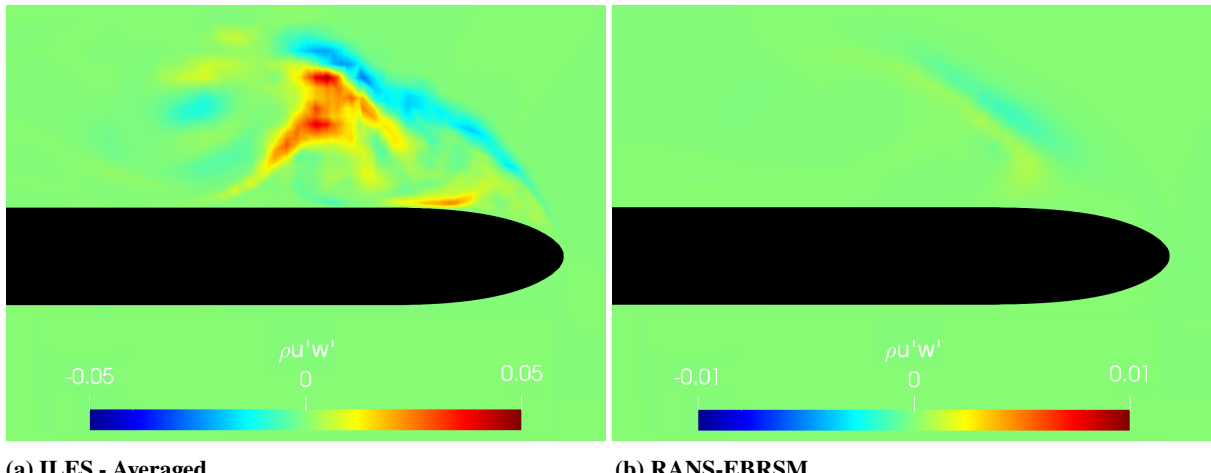


Fig. 9 Contours of streamwise-spanwise Reynolds stress at cross-section $x/c = 0.8$

V. Conclusion

Higher-order flux reconstruction methods were used to simulate the flow around medium-radius and large-radius leading edge VFE-2 delta wings with implicit large eddy simulation. The results of the medium-radius simulation at a Reynolds number of $1 \cdot 10^6$ were found to generally be in very good agreement with the experimental data, although the onset of vortex breakdown was predicted at the trailing edge which was not observed in the experiment. Higher-order ILES of a large-radius leading edge wing at a Reynolds number of 40,000 was then performed for comparison with RANS methods closed with the SST and EBRSM turbulence models. As expected, flow features such as secondary and tertiary vortices were not adequately resolved by RANS methods and the turbulence models severely underpredicted the turbulence in the flow field. As evident in the oil flow paths and total pressure cross-sections, higher-order ILES methods were able to resolve small-scale flow physics that RANS methods could not, but minimal differences in surface pressure distribution were found. Although the complexities of high Reynolds number flow and the large-radius geometry were explored independently, future work will address the more complex physics of the large-radius leading edge at high Reynolds numbers once experimental data at computationally feasible flow conditions exists.

The results showed strong indication that higher-order ILES methods can provide significantly higher fidelity simulations of vortex dominated flows than the industry standard RANS methods. However, the computational costs involved with these higher-order methods are still prohibitively large for common industry use and suffer from distinct drawbacks such as severe time step limitations at high Reynolds numbers for explicit schemes and poor multi-GPU parallelizability due to high memory bandwidth requirements for implicit schemes. Advances in the efficiency of the numerical algorithms must be made before higher-order methods become feasible for industry use.

Acknowledgments

We would like to acknowledge the computational resources and substantial support provided by the Princeton Institute for Computational Science and Engineering (PICSciE) and the Princeton University Office of Information Technology's Research Computing department. In addition, we would like to thank Andrej Furman and Christian Breitsamter of the Institute of Aerodynamics of the Technische Universität München for providing the experimental data for validation of the ILES method.

References

- [1] Mitchell, A., Morton, S., Molton, P., and Guy, Y., "Flow Control of Vortical Structures and Vortex Breakdown over Slender Delta Wings," 2003, p. 15.
- [2] Chu, J., Luckring, J. M., and Center, L. R., "Experimental surface pressure data obtained on 65° delta wing across Reynolds number and Mach number ranges." 1996.
- [3] Furman, A., and Breitsamter, C., "Turbulent and unsteady flow characteristics of delta wing vortex systems," *Aerospace Science and Technology*, Vol. 24, 2012, pp. 32–44.
- [4] Konrath, R., Engler, R., Klein, C., and Kompenhans, J., "Analysis of PSP Results Obtained for the VFE-2 65° Delta Wing Configuration at Sub- and Transonic Speeds," Vol. 2, 2006.
- [5] LE ROY, J.-F., Rodriguez, O., and Kurun, S., Aerospace Sciences Meetings, American Institute of Aeronautics and Astronautics, 2008, Chap. Experimental and CFD Contribution to Understanding Delta Wing Vortical Flow. doi:10.2514/6.2008-380, URL <https://doi.org/10.2514/6.2008-380>, 0.
- [6] Crippa, S., and Rizzi, A., Fluid Dynamics and Co-located Conferences, American Institute of Aeronautics and Astronautics, 2006, Chaps. Numerical Investigation of Reynolds Number Effects on a Blunt Leading-Edge Delta Wing. doi:10.2514/6.2006-3001, URL <https://doi.org/10.2514/6.2006-3001>, 0.
- [7] Cummings, R. M., and Schütte, A., "Detached-Eddy Simulation of the vortical flow field about the VFE-2 delta wing," *Aerospace Science and Technology*, Vol. 24, No. 1, 2013, pp. 66 – 76. doi:<https://doi.org/10.1016/j.ast.2012.02.007>, URL <http://www.sciencedirect.com/science/article/pii/S1270963812000399>, vFE-2.
- [8] Tarhan, E., Ortakaya, Y., Gurdamar, E., and Korkem, B., "PARALLEL NAVIER-STOKES SOLUTIONS OF NASA 65 DEGREE DELTA-WING," 2009, pp. 217–225.
- [9] Crippa, S., and Rizzi, A., "Initial steady/unsteady CFD analysis of vortex flow over the VFE-2 delta wing," Vol. 2, 2006, pp. 883–892.

- [10] Schiavetta, L., Badcock, K., and Cummings, R., Aerospace Sciences Meetings, American Institute of Aeronautics and Astronautics, 2007, Chap. Comparison of DES and URANS for Unsteady Vortical Flows over Delta Wings. doi:10.2514/6.2007-1085, URL <https://doi.org/10.2514/6.2007-1085>, 0.
- [11] SPALART, P., and ALLMARAS, S., Aerospace Sciences Meetings, American Institute of Aeronautics and Astronautics, 1992, Chaps. A one-equation turbulence model for aerodynamic flows. doi:10.2514/6.1992-439, URL <https://doi.org/10.2514/6.1992-439>, 0.
- [12] Menter, F. R., “Two-equation eddy-viscosity turbulence models for engineering applications,” *AIAA Journal*, Vol. 32, No. 8, 1994, pp. 1598–1605. doi:10.2514/3.12149, URL <https://doi.org/10.2514/3.12149>.
- [13] Hesthaven, J. S., and Warburton, T., *Nodal Discontinuous Galerkin Methods: Algorithms, Analysis, and Applications*, 1st ed., Springer Publishing Company, Incorporated, 2010.
- [14] Huynh, H. T., “A Flux Reconstruction Approach to High-Order Schemes Including Discontinuous Galerkin Methods,” 2007. doi:10.2514/6.2007-4079, URL <https://doi.org/10.2514/6.2007-4079>, 0.
- [15] Adams, N. A., and Hicken, S., “Implicit Large-Eddy Simulation: Theory and Application,” *Advances in Turbulence XII*, edited by B. Eckhardt, Springer Berlin Heidelberg, Berlin, Heidelberg, 2009, pp. 743–750.
- [16] Witherden, F., M Farrington, A., and E Vincent, P., “PyFR: An Open Source Framework for Solving Advection-Diffusion Type Problems on Streaming Architectures using the Flux Reconstruction Approach,” 2013.
- [17] Roe, P. L., “Characteristic-Based Schemes for the Euler Equations,” *Annual Review of Fluid Mechanics*, Vol. 18, No. 1, 1986, pp. 337–365. doi:10.1146/annurev.fl.18.010186.002005, URL <https://doi.org/10.1146/annurev.fl.18.010186.002005>.
- [18] Cockburn, B., and Shu, C.-W., “The Local Discontinuous Galerkin Method for Time-Dependent Convection-Diffusion Systems,” *SIAM Journal on Numerical Analysis*, Vol. 35, No. 6, 1998, pp. 2440–2463. doi:10.1137/S0036142997316712, URL <https://doi.org/10.1137/S0036142997316712>.
- [19] Manceau, R., and Hanjalic, K., “Elliptic blending model: A new near-wall Reynolds-stress turbulence closure,” *Physics of Fluids*, Vol. 14, 2002. doi:10.1063/1.1432693.14.10.1063/1.1432693.
- [20] Ims, J., Duan, Z., and Wang, Z. J., “MeshCurve: An Automated Low-Order to High-Order Mesh Generator,” 2015. doi:10.2514/6.2015-2293, URL <https://doi.org/10.2514/6.2015-2293>, 0.
- [21] Zwerger, C., Hicken, S., Breitsamter, C., and Adams, N., “Wall Modeled Large Eddy Simulation of the VFE-2 Delta Wing,” *Direct and Large-Eddy Simulation*, 2018, pp. 289–295. doi:10.1007/978-3-319-63212-4_36.
- [22] Luckring, J. M., and Luckring, J. M., “Reynolds Number and LeadingEdge Bluntness Effects on a 65° Delta Wing,” *AIAA Paper*, 2002.